World Scientific
www.worldscientific.com

CHEMICAL INTERACTIONS AT NOBLE METAL NANOPARTICLE SURFACES — CATALYSIS, SENSORS AND DEVICES

A. SREEKUMARAN NAIR, RENJIS T. TOM, V. R. RAJEEV KUMAR,
C. SUBRAMANIAM and T. PRADEEP*

*DST Unit on Nanoscience, Department of Chemistry
and Sophisticated Analytical Instrument Facility
Indian Institute of Technology, Madras
Chennai-600036, India
pradeep@iitm.ac.in

In this paper, a summary of some of the recent research efforts in our laboratory on chemical interactions at noble metal nanoparticle surfaces is presented. The article is divided into five sections, detailing with (i) interactions of simple halocarbons with gold and silver nanoparticle surfaces at room temperature by a new chemistry and the exploitation of this chemistry in the extraction of pesticides from drinking water, (ii) interaction of biologically important proteins such as Cyt *c*, hemoglobin and myoglobin as well as a model system, hemin with gold and silver nanoparticles and nanorods forming nano–bio conjugates and their surface binding chemistry, (iii) formation of polymer–nano composites with tunable optical properties and temperature sensing characteristics by single and multi-step methodologies, (iv) nanomaterials-based flow sensors and (v) composites of noble metal nanoparticles and metallic carbon nanotubes showing visible fluorescence induced by metal–semiconductor transition.

Keywords: Nanomaterials; halocarbons; nano–bio conjugates; microgels; flow sensors; carbon nanotubes.

1. Introduction

Research on nanomaterials has evinced keen interest in recent years because of the new opportunities they present in nanocomposites, catalysis, environmental remediation and sensing.[1–5] Metal nanoparticles have potential applications in catalysis because of their large surface to volume ratio and unusual chemical reactivity.[6] Metal nanoparticles of different shapes could catalyze the reactions with different efficiencies because nanocrystals of different shapes represent various facets.

---

*Corresponding author.

Nanoparticles of silver, gold, copper, iron and its oxides, palladium and platinum have found applications in catalyzing reactions,[7–11] which offer immense scope for green chemistry. Iron and its oxide nanoparticles are excellent materials for environmental remediation.[4] Nanoscale materials are used as sorbents for contaminants, in nanofiltration and in reactive membranes.[12] The use of metal nanoparticles in sensing could bring about a revolution in biology, healthcare, military and day-to-day life.[13]

In this paper, we present various aspects of our studies on the chemical interactions at noble metal nanoparticle surfaces, touching upon (i) the investigation of the chemical reactivity of Au and Ag nanoparticles towards simple halocarbons by a new chemistry[14–16] and its extension in achieving the removal of common pesticides from drinking water,[17,18] (ii) the immobilization of biologically important proteins on nanosurfaces and their surface binding chemistry,[19,20] (iii) fabrication of polymer polymer–nano composites by single-step methodologies such as polymerization of molecules on nanosurfaces[21] and multi-step strategies,[22–24] (iv) fabrication of flow sensors from metal nanoparticles[25,26] and (v) formation of composites from single-walled carbon nanotubes (SWNT) and noble metal nanoparticles.[27] Simple halocarbons, which pose severe environmental hazards could be degraded by Au and Ag nanoparticles to metal halides and carbon at room temperature.[14] The same chemistry was used as a methodology for making oxide nanobubbles[15] from core–shell nanoparticles and also to investigate the porosity[16] of core–shell nanosystems. The interaction of biologically important proteins such as cytochrome c (Cyt c), myoglobin (Mb) and hemoglobin (Hb) with Au and Ag nanostructures leads to the formation of bio–nano conjugates.[19,20] We have succeeded in bringing about the polymerization of certain molecules such as benzylthiocyanate on nanoparticle surfaces[21] resulting in polymer–nano composites. Temperature sensitive poly (N-isopropylacrylamide)-capped *smart Au nanogels* were recently synthesized.[22] Gold nanorods were grown in microgels, which respond to temperature and pH changes in the environment.[23] Poly (*o*-toluidine) capped Au nanoparticles were synthesized by a one-pot methodology and the utility of the material in pH sensing was explored.[24] An array of Au nanoparticles on conducting glass surfaces was fabricated, which showed excellent flow sensing characteristics.[25,26] Also, composites of Au and Ag nanostructures with carbon nanotubes showed new and exciting phenomena.[27] We will illustrate more detail in the following section.

2. Experimental

Syntheses of citrate-capped Au and Ag nanoparticles and Au nanorods; methodologies for getting nano–bio composites of Cyt c, myoglobin, hemoglobin and hemin with Au and Ag nanoparticles and Au nanorods, polymer–nano composites by single and multi-step processes, fabrication of nanoparticles on conducting glass surfaces for flow sensors, the formation of nanoparticles-nanotubes composites; and the experimental methodology associated with each one of these studies are described

in detail in the cited references. Characterization of the above nanomaterials involved UV–visible spectroscopy (Perkin–Elmer Lambda 25), infrared spectroscopy (Perkin–Elmer Spectrum One), fluorescence spectroscopy (Hitachi F-4500 spectrofluorimeter and Jobin–Vyon fluorolog instrument), Raman spectroscopy (Confocal Raman spectrometer CRM 200 of Witec), matrix assisted laser desorption ionization (MALDI) mass spectrometry (Voyager DE PRO Biospectrometry Workstation of Applied Biosystems), transmission electron microscopy (JEOL 3010 UHR operating at 300 kV), and AFM (CRM 200 of Witec with Alpha SNOM). Samples of extracted metallic SWNT (mSWNT), Au–mSWNT composite and Au–SWNT composites were investigated through point-contact current imaging-atomic force microscopy (PCI-AFM). As-received SWNT samples were thoroughly cleaned to remove impurities. PCI-AFM measurements were done at several places on each of these samples and also across several samples to confirm the authenticity and reliability of the data reported. In case of pure extracted mSWNTs, the sample was drop casted on a freshly cleaved mica surface and allowed to dry in a vacuum desiccator. For composite samples, the material was lifted from the aqueous–air interface (after evaporation of the organic layer) and drop cast on the mica surface. This was also subsequently dried in a vacuum desiccator. Half of the dried samples were masked using a clean cover glass slip and placed inside the thermal evaporation chamber. This chamber consists of a resistive heating wire on which a piece of pure gold metal was placed. The entire chamber was pumped using a turbo–molecular pump to a vacuum of 10^{-6} torr. A quartz crystal plate interfaced to a microbalance unit was held at the same level as the sample, to allow monitoring of the amount and thickness of the gold layer deposited. After pumping the system to vacuum, the evaporation of the gold was carried out by increasing the current through the resistive wire. This causes the gold to evaporate and deposit all around the evaporation chamber, including the unmasked portion of the sample. The evaporation was carried out till a gold pad thickness of 30–40 nm was achieved on the sample, which was monitored using the quartz crystal. The evaporation was then stopped and the chamber was brought slowly to room temperature with constant pumping. Finally, the samples were removed from the chamber, the mask was lifted carefully and the samples were preserved until further use.

PCI-AFM measurements were carried out on a JEOL JSPM-4210 instrument equipped with two function generators (WF 1946, NF Corporation). The I–V characteristics along the long axis of the nanotube composite were measured using Pt-coated conductive cantilevers. From the large area topographic image, it was ensured that the tubes selected for I–V measurements were indeed in contact with the gold electrode. The bias voltage was applied on the gold electrode and the cantilever was grounded. The entire experiment was carried out in a housing purged with N_2 gas to minimize the effects of humidity. The I–V data corresponds to the point of contact which reflects the local symmetry. The PCI-AFM image was constructed for 128×128 pixels with topographic and I–V characteristics acquired simultaneously.

3. Results and Discussion

3.1. *Interaction of halocarbons with metal nanoparticle surfaces — a novel chemistry for environmental remediation*

We have invented new reactions between the nanoparticles of Au and Ag (details are described in Ref. 14) and simple halocarbons such as CCl_4, $CHBr_3$, CCl_3F and benzylchloride, whereby the halocarbons are degraded by the nanoparticles to metal halides and amorphous carbon at room temperature.[14] We have systematically investigated the reactions in detail by spectroscopy, microscopy, pH and conductivity measurements to gain an understanding of the mechanistic aspects of the degradation. We have noted that the Au and Ag nanoparticles degrade the halocarbons by different reaction pathways.[14] While the halocarbons directly react at the nanoparticle surfaces in the case of Ag, they adsorb onto the surfaces of Au nanoparticles and degrade completely over a period of time, bringing about interesting features in the surface plasmon characteristics. The chemical reactivity of Au and Ag towards the halocarbons and the corresponding changes to the surface plasmon feature of the nanoparticles were monitored by UV–visible spectroscopy in a time-dependent manner. These are illustrated in Fig. 1. Figure 1(a) is the UV–visible spectra showing the interaction of Ag nanoparticles (70-nm diameter) with CCl_4. The progressive reduction in the intensity of the surface plasmon peak is attributed to the time dependent conversion of Ag into AgCl by CCl_4. Complete conversion of Ag into AgCl occurs in 12 h of interaction. The interaction of halocarbons with Au ($\sim$15 nm diameter) follows a different pathway, as is evident from Fig. 1(b). The binding of the halocarbon (benzylchloride) on Au results in time-dependent changes in the surface plasmon feature due to the adsorbate-induced aggregation of the nanoparticles.[14] The adsorbate-induced aggregation of Au nanoparticles was confirmed by TEM studies. The adsorbed halocarbons then react with the Au nanoparticles over a period of 48 h, resulting in their complete degradation to $AuCl_3$ and amorphous carbon. The formation of metal halides (AgCl and $AuCl_3$) was confirmed by X-ray diffraction and absorption spectroscopy respectively, and amorphous carbon by infrared (IR) and Raman spectroscopy.[14] The insets of Figs. 1(a) and 1(b) are the photographs depicting the color changes before (left) and after (right) the reaction with the respective nanoparticles. The pH and conductivity during the course of the reaction were monitored in a time-dependent manner. The pH of the reaction showed a decrease from 9.7 (that of the starting reaction mixture) to 1.2 (after complete degradation) during the course of the reaction and the conductivity of the solution showed a marked increase from $3.32 \times 10^3 \, \mu S \, cm^{-1}$ to $3.51 \times 10^4 \, \mu S \, cm^{-1}$. The conversion of 2-propanol (in the reaction mixture) to acetone (CH_3–CHOH–CH_3 $\rightarrow$ CH_3–CO–CH_3+2H$^+$+2e, the formation was confirmed by gas chromatographic measurements) *via* ketyl radical formation during the reaction is supposed to be the main source of protons. Hence the reason for the drastic reduction in pH. The chemical reactivity was also investigated with other halocarbons such as benzylchloride,
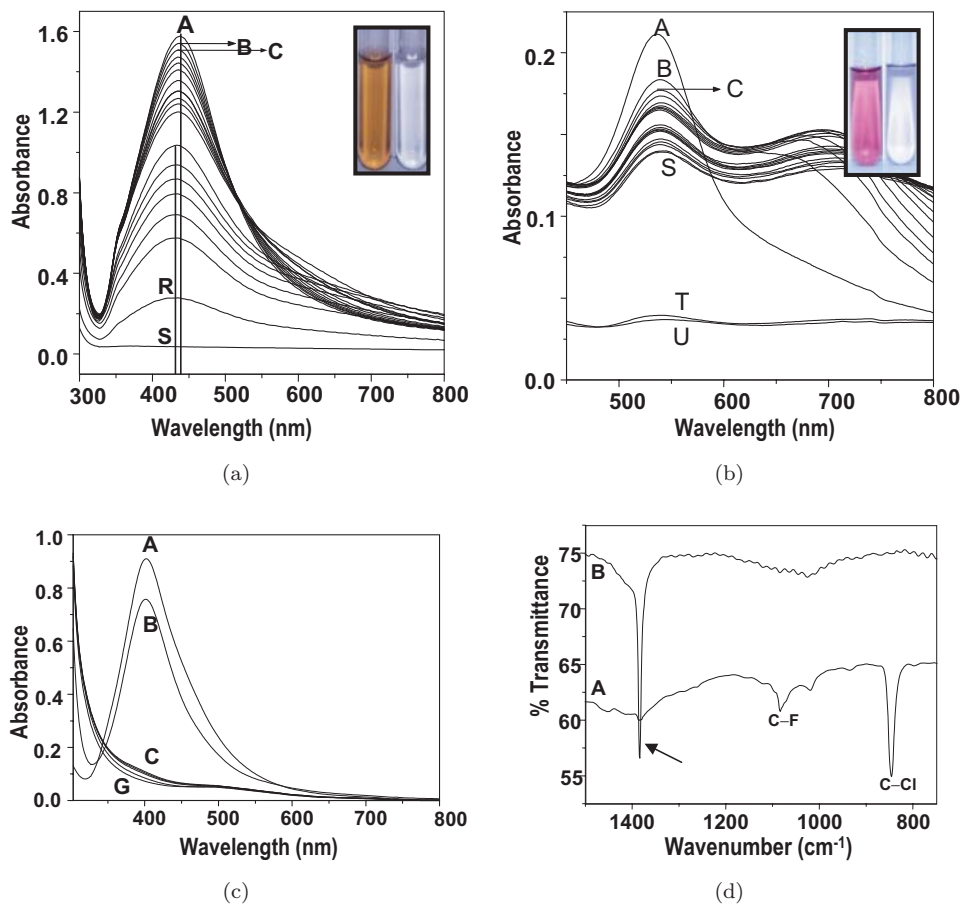
(a)

(b)

(c)

(d)

Fig. 1.   (a) Variation in the UV–visible spectrum of silver nanoparticles upon the interaction with CCl$_4$. Spectrum of the pure nanoparticles, (A) shows the plasmon excitation at 438 nm, characteristic of silver nanoparticles of 60–80 nm diameter. Trace (B) was recorded just after the addition of 50 μL of CCl$_4$ to 2.5 mL of the solution. Subsequent traces were taken at 20 mins intervals (C to R) and trace (S) was recorded after 12 h showing the complete disappearance of the plasmon excitation. (b) Changes in the absorption spectra during the reaction between Au@citrate and benzylchloride. Trace (A) is the absorption spectrum of pure Au@citrate. Trace (B) was taken immediately after the addition of benzylchloride. Subsequent traces, (C–S) were taken at 20 mins intervals. The absorption spectrum U was taken after 48 h. (c) UV–visible spectra of the reaction between Ag@citrate and CHBr$_3$ in a time-dependent manner. The traces were taken at intervals of 3 mins. Note the rapid decrease in the intensity of the plasmon excitation of Ag@citrate (A) by the addition of 50 μL of bromoform to 2.5 mL of Ag@citrate (B–G). (d) A comparison of the infrared spectra of CCl$_3$F (trace A) and its reaction product with Ag@citrate (trace B). Note that the C–Cl and C–F features disappeared in the reaction product and a sharp peak corresponding to amorphous carbon emerged (indicated by an arrow) at 1384 cm^{-1}.

CH_2Cl_2, $CHBr_3$ and CCl_3F. The kinetics of binding and degradation of benzylchloride with Ag and Au were found to be faster compared to the CCl_4 case. The fastest reaction observed was with $CHBr_3$. Figure 1(c) shows the time-dependent UV–visible spectra of the reaction between $CHBr_3$ and Ag. The surface plasmon peak of Ag disappears just after 10 mins of their interaction. In the degradation of CCl_3F, analysis of the reaction product (Fig. 1(d), trace B) by infrared spectroscopy revealed the complete disappearance of the C–F and C–Cl bonds (seen in CCl_3F, Fig. 1(d), trace A) and the appearance of the carbonaceous peak (indicated by arrow). Similarly, no C–H frequency was seen in the reaction products of CH_2Cl_2 and $CHCl_3$ indicating their complete degradation. In view of the mechanistic details of the reaction investigated, the degradation reaction in the case of Ag may be represented as $(4Ag_{(s)} + CCl_{4(l)} \rightarrow 4AgCl_{(s)} + C_{(graphite)}$, $\Delta H = -379.8$ KJ mol^{-1}, considering $\Delta H^0_{f\,298}$ of CCl_4 and AgCl as -128.2 and -127.0 kJ mol^{-1}, respectively). The large negative ΔH value accounts for the fast reaction of halocarbons with the Ag nanoparticles. Thermochemistry suggests a less exothermic reaction $(4Au_{(s)} + 3\,CCl_{4(l)} \rightarrow 4AuCl_{3(s)} + C_{(graphite)}$, $\Delta H = -85.8$ kJ $mol^{-1})$ for gold, $(\Delta Hf^o_{298}$ for $AuCl_3 = -117.6$ kJ $mol^{-1})$ which could be the reason for the slow reaction between Au nanoparticles and the halocarbons. The chemistry of halocarbons with metal nanoparticles was used to selectively leach metal cores from core–shell nanoparticles, namely $Ag@ZrO_2$, $Au@ZrO_2$ and $Au@SiO_2$ (metal cores protected with oxide shell of ZrO_2 and SiO_2, respectively).

The selective removal of Au and Ag nanoparticles resulted in ZrO_2 and SiO_2 nanobubbles/nanoshells.[15,28] The reaction of CCl_4 with $Au@SiO_2$ nanoparticles resulted in the growth of carbon onions inside the SiO_2 shell.[28] The halocarbon chemistry was also used to investigate the porosity of the shells.[16] This novel chemistry opens up a feasible means to incorporate molecules in nanoshells and investigate their spectroscopy in a confined atmosphere.[29] The methodology also enables us to incorporate drugs in nanoshells and study their controlled delivery.[30]

While searching for a feasible field of application for this new chemistry, the pesticide contamination in drinking water in India and some parts of the world came to our attention. Incidentally, most of the pesticides of interest (those detected in water) are either halocarbons or molecules with sulfur. These pesticides are endosulfan, chlorpyrifos and malathion, their presence in drinking water and soft drinks has become a huge environmental issue in India. Our initial experiments were using bare nanoparticles for their detection and extraction from water. Figure 2(a) shows changes to the absorption spectrum when endosulfan of different concentrations was exposed to Au nanoparticles.[17] The resultant color change is shown in the inset. The decrease in the intensity of the surface plasmon feature at 532 nm and the concomitant emergence of absorption peaks at longer wavelengths is characteristic of adsorbate-induced aggregation of the nanoparticles (and the resultant inter-plasmon coupling). This is clearer in Fig. 2(b), which shows the time-dependent UV–visible spectral changes of the interaction of endosulfan with Au nanoparticles. Note the reduction in the intensity of the 532 nm peak and the emergence of
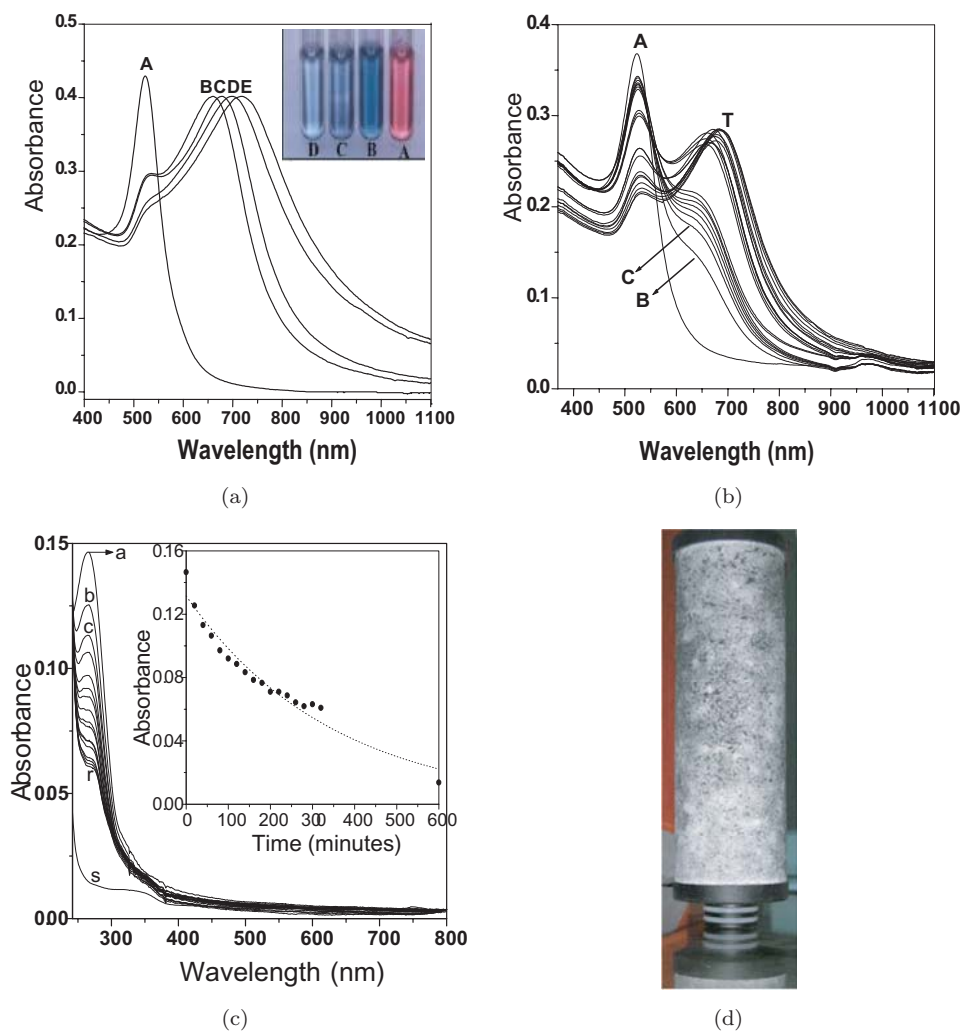
(a)

(b)

(c)

(d)

Fig. 2. (a) UV–visible spectrum of (A) citrate stabilized gold nanoparticles and the effect of exposure of endosulfan at various concentrations: (B) 2 ppm, (C) 10 ppm, (D) 100 ppm, and (E) 250 ppm. The spectra were recorded 9 h after exposure to endosulfan. The solutions have the same composition, except for endosulfan. A photograph of the solutions is shown in the inset, (A) pure citrate stabilized nanoparticles; (B), (C) and (D) correspond to 2, 10 and 100 ppm, respectively. (b) Time-dependence of the UV–visible absorption spectrum of citrate stabilized gold nanoparticles upon exposure of 10 ppm endosulfan. (A) Original nanoparticle solution, (B) 3 mins after adding endosulfan solution, (C) to (T), at 20 mins intervals thereafter. (c) shows the time-dependent UV–visible spectra showing the adsorption of 1 ppm chlorpyrifos on Al_2O_3@Ag. Trace A is the absorption spectrum of 1 ppm chlorpyrifos and traces (B–R) were taken at 20 mins intervals after the interaction with the nanoparticles. Trace s was taken after 10 h showing the complete disappearance of chlorpyrifos from water. The inset shows decrease in absorbance vs. time from the absorption spectroscopy data for the traces (A–S). The dotted line in the inset shows a fit of the exponential decrease in absorbance with time. (d) Photograph of a pesticide filter devise using supported nanoparticles.

another absorption peak at longer wavelength in a time-dependent manner. The binding of endosulfan on Au and Ag was also confirmed by spectroscopic means. Similarly, we have found that chlorpyrifos and malathion also bind to the nano surfaces effectively.[18] Having established the binding of pesticides on nano surfaces, we thought of making a pesticide filter by the incorporation of nanoparticles on suitable supports for water purification purposes. Activated alumina is a good adsorbent and a known player in water purification area. The activated alumina-supported Ag and Au nanomaterials were used for pesticide removal studies and device fabrication. Figure 2(c) shows the time-dependent UV–visible spectra of the interaction of chlorpyrifos with the supported nanoparticles of Ag.[18] Complete uptake of the pesticide by the supported nanoparticles occurs after 10 h of their interaction. This kind of an approach was used for column studies in which the nanoparticle loaded alumina was loaded in a column. Pesticide-spiked water was passed through at 50 ppb concentration and complete removal was detected using gas chromatography using electron capture detection. Taking data from such studies, we devised a filter (Fig. 2(d)), which is now in the market as part of a domestic water purifier.

3.2. *Interaction of biomolecules with nanoparticles-formation of nano–bio conjugates*

Nano–bio conjugates represent a class of interesting materials having widespread applications in gene and drug delivery. A study of chemical interactions of biomolecules with nanosurfaces is important as the conformations and hence the biological activity of the biomolecules could be modified by the interactions. We have investigated the chemical interactions of biologically important molecules such as Cyt *c*, hemoglobin (Hb) and myoglobin (Mb) on Au and Ag nanostructures resulting in the formation of nano–bio conjugates.[19,20] In order to study the interaction of the protein and the effect of such interactions on the functions of the active site, a model system, namely hemin was used. In the case of Au, experiments were conducted with ∼15 nm particles, whereas for Ag, ∼ 4 nm (hereafter Ag(I)) and ∼ 70 nm (hereafter Ag(II)) particles, synthesized by standard methodologies, were employed. Figure 3 shows UV–visible traces of the nano–bio conjugates of hemin with Au (Fig. 3(a)) and Ag (Fig. 3(b) and Fig. 3(c)). Both the Ag nanoparticles showed more aggregation tendency after hemin binding compared to the Au nanoparticles owing to the presence of carboxyl groups in hemin (Ag has more affinity towards –COOH groups), which make particle interlinking feasible. On the other hand, the surface plasmon feature of Au is well defined even after hemin binding, the corresponding feature of Ag is broadened, indicative of aggregation due to greater interaction between particles. The peak maxima of Ag(I) and Ag(II) particles are shifted to higher and lower values as a result of the interaction. Figure 3(d) shows time-dependent UV–visible traces of the interaction of Ag(I) with hemin, the traces being taken at an interval of 10 mins. Shape changes in the surface plasmon band indicate the formation of aggregates of the nano–bio conjugates.
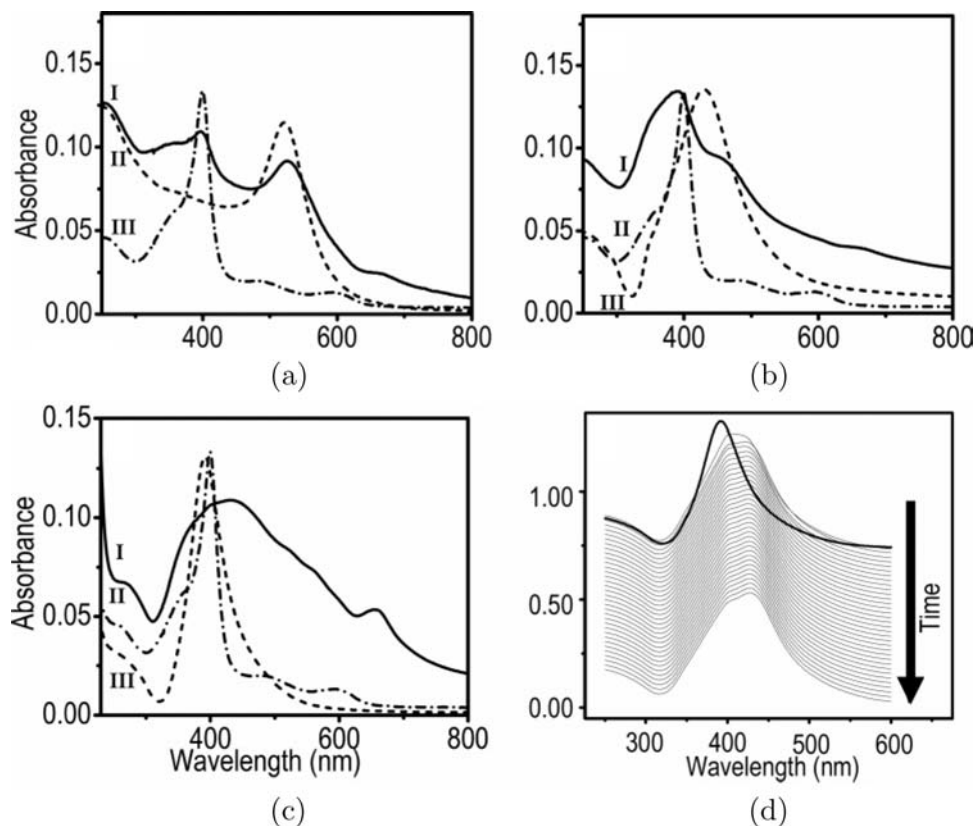
Fig. 3.   (a–c). UV–visible spectra of Au, Ag (II), and Ag (I) particles, respectively taken in 20% aqueous ethanol. Traces (I), (II), and (III) represent the Hem capped nanoparticles, M@Hem, citrate capped nanoparticles, M@Cit and 0.004 mg/mL hemin chloride, respectively. (d) Time dependent binding of Hem on Ag (4 nm) particle monitored at a time interval of 10 mins for the initial 6 h. Thick curve in (d) corresponds to the parent nanoparticle solution. Traces has been offset for clarity.

Figure 4 illustrates the absorption and emission spectra of Cyt *c* bound Au (Au@Cyt *c*, Figs. 4(a) and 4(b), respectively) and Ag (Ag@Cyt *c*, Figs. 4(c) and 4(d), respectively) nanoparticles. Traces I, II and III in Figs. 4(a) and 4(c) denote the absorption spectra of Cyt *c* bound nanoparticles, citrate capped nanoparticles (showing the surface plasmon resonance) and, pure Cyt *c* (showing a strong Soret band at 408 nm and a weak Q-band at 540 nm), respectively. The binding of Cyt *c* to the nanoparticles results in changes in the dielectric constant of the neighboring environment and hence the red-shift in the surface plasmon band. Figure 4(c) details the broadening and shift in the surface plasmon band of Ag as a result of Cyt *c* binding. Figure 4(d) shows an enlarged view of Fig. 4(c) in the region 350–480 nm, showing the shift in the peak maximum clearly. Figure 4(b) shows the fluorescence spectra of Cyt *c* and Au@Cyt *c* conjugates, respectively. The emission maxima for
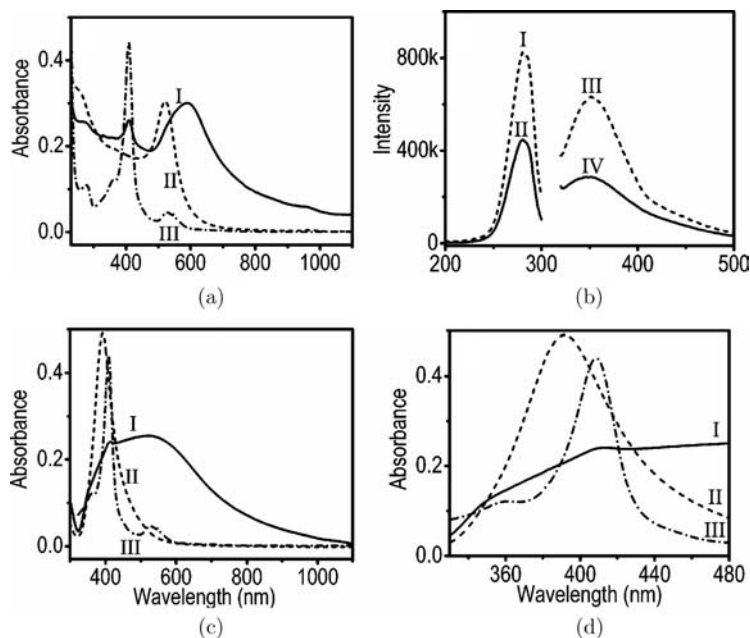
Fig. 4.   (a) and (b) Absorption and emission spectra, respectively of the Au@Cyc system. Traces (I), (II), and (III) correspond to 0.2 mg/mL Au@Cyt *c*, 0.1 mg/mL Au@Cit and 0.1 mg/mL Cyt *c*, respectively. (B) Excitation and emission spectra of [(I) and (III)] free Cyt *c* (0.01 mg/mL) and [(II) and (IV)] Au@Cyt *c* (0.05 mg/mL) taken in water. (c) is the absorption data of the Ag(I) nanoparticle system. The traces (I), (II), and (III) correspond to similar systems as in A. (d) An enlarged view of panel C in the region, 350–480 nm.

both Cyt *c* (trace III) and Au@Cyt *c* (trace IV) are at 532 nm, and the absence of shifts in the excitation and emission features of free Cyt *c* and the conjugate indicates that the fluorophore is away from the surface of the nanoparticles. The decreased fluorescence is because of quenching of the excited flourophore by the nanoparticles. The nano–bio conjugates were characterized by TEM, IR, Raman spectroscopy and matrix assisted laser desorption ionization (MALDI) mass spectroscopy. TEM images indicated well-separated nanoparticles in the case of Au, whereas aggregated structures in the case of Ag. Infrared and Raman spectra gave spectroscopic signatures of the binding of the biomolecules on Au and Ag. Similarly, we have investigated the formation of bioconjugates from myoglobin (Mb) and hemoglobin (Hb) with Au (Au@Mb) and Ag (Ag@Mb) nanostructures. The conjugates were characterized by absorption spectroscopy. The UV–visible spectra of the bioconjugates showed the Soret band of Mb and Hb at 408 and 407 nm, respectively. The surface plasmon band of Au red-shifted from 520 nm to 543 nm and 527 nm, respectively after the binding with Mb and Hb. UV–visible spectra of Ag@Mb and Ag@Hb showed broad peaks due to aggregation of the conjugates. The nano–bio conjugates formed were further characterized by TEM, IR, Raman, and MALDI techniques. TEM images showed well-separated particles in the case
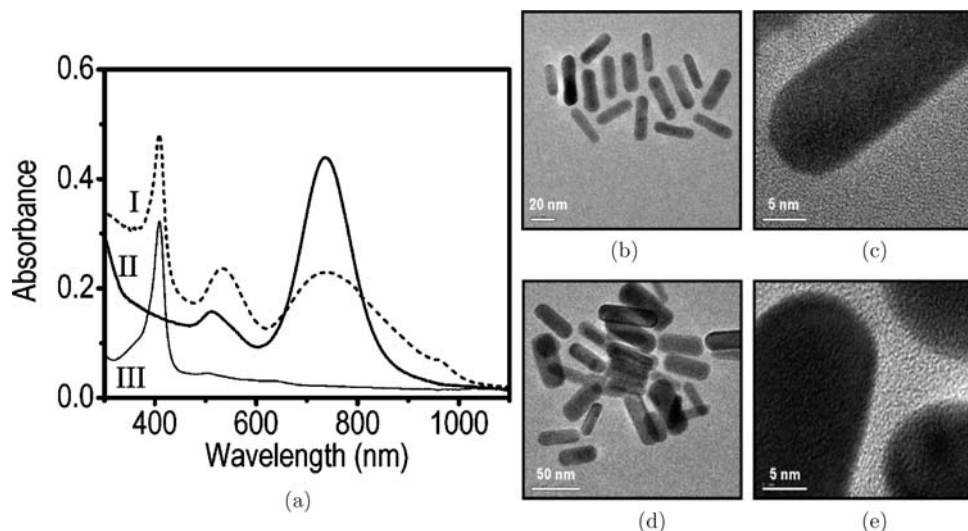
Fig. 5. (a) UV–visible spectra of AuNR@Mb (I), pure AuNR (II), and Mb(III) 0.1 mg/mL in PBS. HRTEM images of neat AuNR (b, c) and AuNR@Mb (d, e). Images (c) and (e) are lattice resolved.

of Au and aggregated structures in the case of Ag. Infrared and Raman spectra showed the spectral features of the biomolecules on the nanosurfaces. The spectral features of the biomolecules in the nano–bio conjugates were broadened and red-shifted compared to the pure biomolecules, indicative of their surface binding.

We have also studied the conjugate formation of Mb with Au nanorods (AuNR@Mb). This is shown in Fig. 5. Traces I and II correspond to the absorption spectra of AuNR@Mb and pure AuNR solution, respectively (Fig. 5(a)). The AuNRs show two absorption bands at 510 and 736 nm, respectively, corresponding to the transverse and longitudinal plasmons (trace II). After binding to Au, the surface plasmon bands are shifted to 534 and 740 nm, respectively. The dampening and broadening of the longitudinal plasmon is due to aggregation of the nanorods as a result of biomolecule binding. This is further illustrated in the HRTEM images (Figs. 5(b)–5(e)). Figures (5(b), 5(c)) and (5(d), 5(e)) show the TEM images of pure Au nanorods and AuNR@Mb bioconjugates, respectively. As can be seen, the conjugate showed aggregate structures, further confirming the observations in the UV–visible spectra. The protein binding did not cause any change in the morphology of the nanorods, as can be seen from the high-resolution images in Figs. 5(c) (before binding) and 5(e) (after binding).

3.3. *Formation of nanomaterials-polymer composites*

Nanomaterials–polymer composites provide enormous flexibility in devising smart materials with advantageous optical, electrical and mechanical properties. We have explored the possibility of making nanoparticle–polymer composites by single and

multi-step methodologies. Our investigations revealed that benzylthiocyanate poly-merizes on Ag nanoparticle surfaces to give a nanoparticle–polymer composite (here-after Ag@PBT) at room temperature.[21] The Lewis acidity of the Ag^+ ion was used to initiate the polymerization reaction. The composite formed was characterized by spectroscopy and microscopy. We also tried to tune the optical properties of the core–shell material by increasing the shell thickness. This was achieved by start-ing the reaction with a larger concentration of benzylthiocyanate. As expected, the plasmon position showed a red-shift with increasing the thickness of the shell. The surface plasmon is very sensitive to the core radius and shell thickness. Since the core size remains invariant, the growth of the shell around the silver core is the main reason for the red-shift observed in the UV–Vis spectrum. The robustness of the polymeric shell for ion permeability was checked by treating the core–shell material with cyanide ions. The shell did not allow the ions to permeate and react with the metal core. This is shown in Fig. 6(a). Up to $2\,mM\ CN^-$, the core was stable. How-ever, at larger ionic concentration, the core is completely destroyed within several minutes. The gradual build up of a thick polymeric shell around the nanoparticles' surfaces caused a red-shift in the surface plasmon peak to higher values. The new position of the surface plasmon peak coincides with the wavelength of the laser line used to measure the Raman spectrum leading to a resonance enhancement in the Raman signal. The Raman spectrum of the composite measured using the resonance enhancement is shown in Fig. 6(b). The intense Raman line at $1600\,cm^{-1}$ due to –C=N– was used to image the material. The Raman image generated using the $1600\,cm^{-1}$ line is shown in the inset of Fig. 6(b). Since the Raman imaging is a
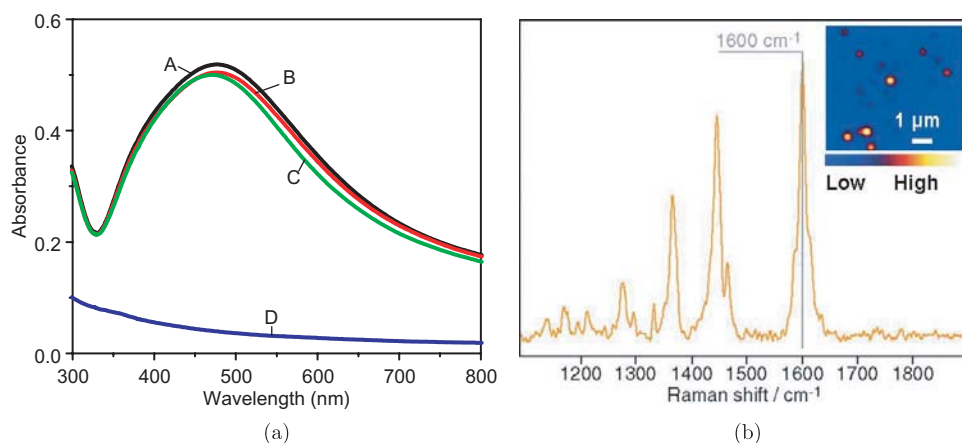

(a)

(b)

Fig. 6.   (a) UV-vis spectrum of Ag@PBT treated with cyanide in water- isopropyl alcohol mixture. The silver core remained stable even for a day in $2\,mM$ NaCN. Curve A indicates the UV–vis spectrum of Ag@PBT in water-isopropyl alcohol mixture. Curve B is the UV–vis spectrum of Ag@PBT measured 1 h after the addition of $2\,mM$ CN and curve C is after 24 h. Curve D is after adding $10\,mM$ $NaCN^-$. (b) shows the Raman spectrum of Ag@PBT. Inset shows Raman image of the material generated by summing up the intensity at $1600\,cm^{-1}$.

low-resolution technique, it was not possible to image the core–shell geometry of a single particle. However, the image showed aggregates of core–shell structures. The intensity was maximum at the center of the aggregate and fading away as we move to the periphery of the aggregate, which is expected for a collection of particles. Protons generated from the conversion of isopropyl alcohol to acetone via the formation of ketyl radicals are supposed to bring about the polymerization of benzyl thiocaynate.

Functional polymers such as poly(N-isopropyl)acrylamide (PNIPAm) can be used to incorporate metal nanoparticles inside them. Such polymers can form large particles of well defined shape. We have succeeded in making gold nanorod patterns using PNIPAm microgels by a template assisted method.[23] CTAB-capped Au nanoparticles were used as seed particles to grow nanorods over the microgel particles. 2 mL of the purified microgel dispersion was mixed with the same volume of the nanoparticle seed solution and left undisturbed for adsorption for sufficient time. The nanoparticle-adsorbed microgel, removed by centrifugation, was analyzed by absorption spectroscopy and TEM. The seed loaded microgel was kept in a growth solution containing 40 mL of 100 mM CTAB, 1.7 mL of 10 mM $HAuCl_4 \cdot 3H_2O$, 250 μL of 10 mM $AgNO_3$ and 270 μL of 100 mM ascorbic acid. This results in the growth of nanorods on the surface of the microgels. The nanorod-coated microgel was separated by centrifugation and analyzed by spectroscopy and microscopy. The microgel structures showed a larger population of nanorods at the periphery as the TEM image is a two-dimensional projection. A large area image of the nanorod-loaded microgel is shown in image (I) of Fig. 7(a). Image (II) shows a single microgel decorated with nanorods. A high-resolution image of an adsorbed nanorod is shown in (III). We allowed the microgel to self assemble by keeping the same in water for two days. The UV–visible spectrum of the material showed transverse and longitudinal plasmon bands of nanorods, which are red-shifted compared to the nanorod-coated microgel due to greater interaction between the nanorods in the self-assembled structure. A large area image of the hexagonal pattern is shown in the image (I) in Fig. 7(b). In the self-assembled pattern, each microgel particle was surrounded by six others. A large area image of the hexagonal pattern with the defect sites marked with white circles is shown in the image (iii) in Fig. 7(b). A schematic of the self-assembly is shown in Fig. 7(c). The spherical microgel particles change to hexagonal in shape during self-assembly to fill the voids. The material showed regions with the absence of nanorod marking. The polydispersity of the prepared microgel contributed to defects.

We have found that redispersible nanocomposites of gold nanoparticles and nanorods could be made by using PNIPAm.[22] Trace *a* in Fig. 8(a) shows the UV–Vis spectrum of gold nanoparticle-PNIPAm hydrogel in water below the transition temperature and trace B corresponds to that of the dispersion above the phase transition temperature. Trace C is after bringing the solution back to the initial temperature. The UV–Vis spectrum of the material showed surface plasmon resonance peak around 520 nm, characteristic of gold nanoparticles. The sample above
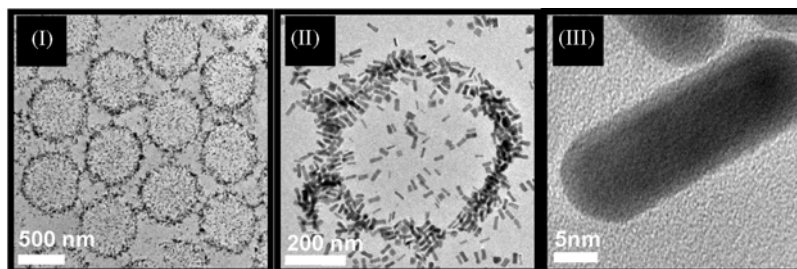
(a)
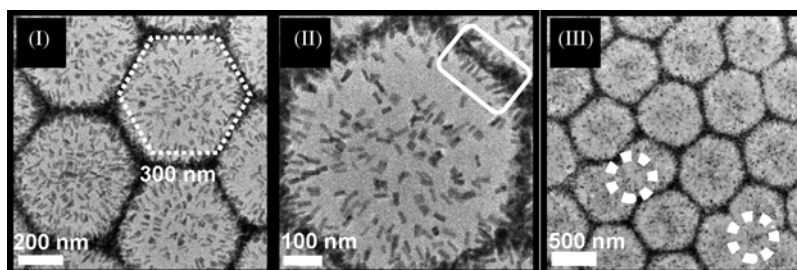
(b)
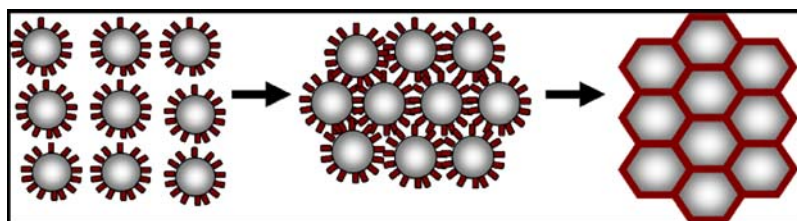
(c)

Fig. 7.   (a) Image (I) shows the large area image of the nanorod-coated microgels. The decoration of microgels by nanorods at the periphery is clear in image (II). A high resolution TEM image of nanorod part of microgel is given in image (III). (b) Image (I) shows the large area image of a hexagonal pattern. The rectangle in (II) shows the largely parallel arrangement of nanorods at the junction. A large area image of the hexagonal pattern with defects is given in (III). The defect sites are shown by dashed circles. Schematic showing the formation of a hexagonal pattern by the fusion of nanorod-coated microgels is shown in (c).

the transition temperature ($32°C$) showed increased absorption. This is attributed to scattering due to the precipitation of the polymer from the solution. The solution after switching ($25°C$) came back to the initial condition, indicating the reversible nature of the switching. Photograph in the inset of Fig. 8(a) shows the color change of the solution during switching. The color of the solution changed from wine red to opaque red during the phase transition. Interestingly, the solution does not show any drastic color change, which is expected when nanoparticles aggregate. This indicates that shrinking of the gel does not reduce the inter-particle distance below the limit necessary for plasmon coupling. The switching can be repeated any number of times.
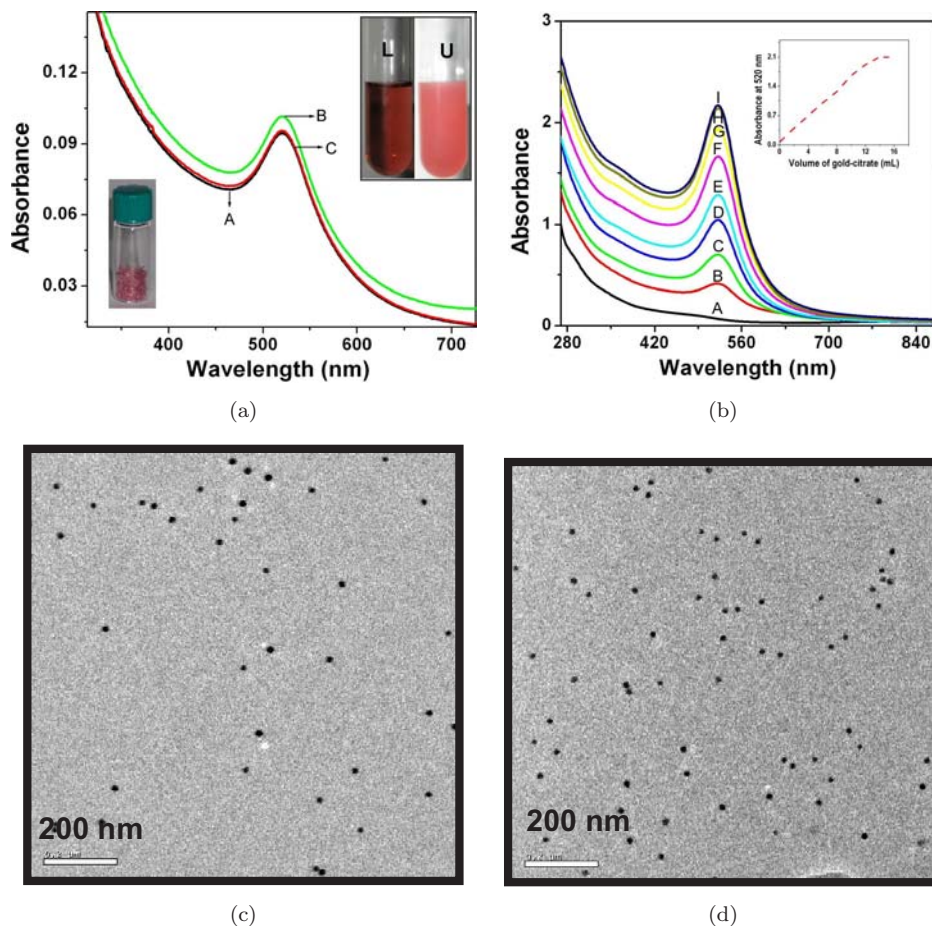
Fig. 8. (a) The UV–Vis spectrum of gold nanoparticle–PNIPAm composite. Trace A is before switching. Trace B is above the phase transition temperature, showing significant scattering. Trace C is after cooling the solution to room temperature, showing complete reversibility. The inset shows the photograph of the material below (L) and above (U) the phase transition temperature. Inset in (a) at the bottom left shows the photograph of the dried composite after one time loading of the nanoparticles. (b) shows the UV–Vis spectrum of the gold nanoparticle–PNIPAm composite showing the effect of loading. Traces (A–I) correspond to repeated loading of the same amount of nanoparticle with the same gel. Inset shows the intensity of the surface plasmon peak as a function of nanoparticle loading, (c) shows the TEM image of the gold nanoparticle–PNIPAm composite after first loading and (d) after saturation loading.

The bottom inset in Fig. 8(a) shows a photograph of the vacuum dried sample. To get an idea about the empty space inside the gel and to see whether the material shows any change in the electronic properties with the nanoparticle concentration, the material was loaded repeatedly with gold nanoparticles. Figure 8(b) shows the UV–Vis spectrum of the material during each loading. 2 mL of the gel was found to take up 14 mL of gold citrate solution. This material will have approximately

17.734×10^9 gold nanoparticles inside the voids. The uptake of nanoparticles into the gel (Fig. 8(c) is the TEM image of the gel after first loading of the nanoparticles) was linear and the gel showed a saturation loading as seen from the leveling of the absorbance at the plasmon peak position. As we can see from the TEM image of the gel after saturation loading (Fig. 8(d)), particles do not interact with each other. As a result, the absorption spectrum shows no shifts upon repeated loading. The same experiment was repeated with the gold nanorods. The position of both longitudinal as well as transverse peak remained the same throughout the switching even though the intensity increased, which indicates that the inter-particle interaction is very weak in the case of gold nanorod–PNIPAm composite. The switching was reversible as concluded from the position as well as the intensity of both the longitudinal and the transverse peaks. For the composite made from CTAB capped gold nanorods, saturation-loading experiments were performed. $250\,\mu L$ of the as prepared gel was found to absorb $25\,\mu L$ of the gold nanorod solution. This amounts to a loading of 3.07×10^{10} gold nanorods into $250\,\mu L$ of the gel.

3.4. *Nanoparticle-based flow sensors-transverse electrokinetic effect*

We report the generation of a potential difference due to flow of a liquid across a metal nanoparticle multilayer assembly. The nanoparticles are self-assembled on an indium doped tin oxide conducting glass plate (ITO) by covalent interactions and characterized by UV–visible absorption spectrophotometry. A device is fabricated by arranging two ITO plates, one containing the nanoparticle assembly and the other without it, with their conducting surface facing each other. The edges are separated by a thin inert spacer so that the two conducting surfaces are not in direct contact. Electrical leads taken from the conducting surfaces are connected to the terminals of a Keithley 2700 digital multimeter for online data acquisition and storage. The schematic of the experimental setup is shown in inset (I) of Fig. 9. We find that a potential difference is generated when a liquid flows across the nanoparticle assembly. This potential difference is generated in a direction transverse to the direction of the flow. The magnitude of the potential difference is found to depend on various factors such as the flow rate, dipole moment, viscosity and ionic concentration of the flowing analyte liquid. It is also found to be dependent on the surface coverage of the nanoparticles on the ITO plate. A plot of potential difference generated for various flow rates, with water as the analyte liquid, is shown in Fig. 9. Similar calibration plots could be generated for other parameters like dipole moment, viscosity, ionic concentration and surface coverage. Interestingly, the phenomenon could be observed with other metal nanoparticle assemblies like that of silver (mean diameter 60 nm) and gold nanorods (diameter 11 nm, aspect ratio 2.8). However, nonmetallic systems such as SiO_2 assemblies failed to show this effect. Control experiments done with two ITO plates neither of them containing the
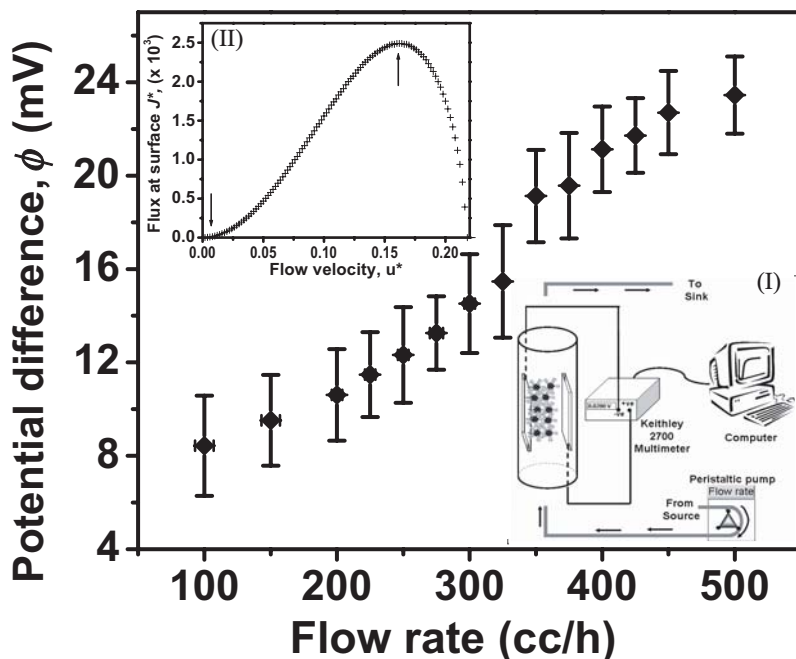
Fig. 9. Variation of potential difference as a function of flow rate for triply distilled water. Inset (I): A schematic of the experimental setup. The device is suspended inside a cylindrical glass column through which the analyte liquid is circulated from the bottom using a peristaltic pump. Inset (II): A plot of flux generated at the surface as a function of flow velocity. The arrows represent the experimentally relevant flow regime. The calculations are done in a numerical manner with dimensionless quantities.

nanoparticles, failed to produce potential difference. Efforts to measure the potential difference in a longitudinal direction (to the flow) also yielded negligible values. Potential difference could not be observed for the device suspended in still water. Through all these control experiments, we attribute this effect solely to the liquid flow across the metal nanoparticle assembly. Based on an elaborate set of experiments, a semi-classical qualitative theoretical understanding of the phenomenon is achieved.

The model considers a single isolated nanoparticle grafted on the ITO surface. The dipole of the flowing liquid interacts with the surface charges of the nanoparticle resulting in a momentum impulse and the subsequent transfer of energy from the flowing dipole to the surface charge on the nanoparticle.[31] Several such Columbic collisions cause the charge to be ejected from the nanoparticle surface with a definite kinetic energy. The ejected charges experience the effect of (a) the viscous drag of the flowing liquid, (b) the electrostatic attraction by the charged nanoparticles and (c) a steeply repulsive interaction preventing the charge from reaching the nanoparticle surface. The combined effect of all these would lead to the charge (which is solvated by the analyte liquid) reaching the surface of the ITO plate with a velocity. This

velocity is used to calculate the flux of charges at the surfaces, which is proportional to the potential difference observed. The validity of this theoretical model is seen when the flux of the charges at the ITO surface is plotted as a function of the flow rate of the analyte liquid, as shown in inset (II) of Fig. 9. Excellent agreement with the experimental observation is seen, for the region marked within the arrows in inset (II) of Fig. 9. Similar agreement is observed with dipole moment and viscosity, thereby validating the theoretical model.

3.5. *Visible fluorescence from metal nanoparticle–single walled carbon nanotube composites*

We have reported that as a result of interaction between nanoparticles and SWNT to form a composite, the latter emits in the visible region of the electromagnetic spectrum. The composites, prepared by the interaction of purified SWNTs and metal nanoparticles at the liquid–liquid interface, were probed using micro Raman spectroscopy. The usual Raman modes of SWNTs like the RBM, D, G and G' bands were observed along with a sharp visible emission, as shown in Fig. 10. Further studies, using varying excitation sources, established the emission to be fluorescent in nature. The strong fluorescent signal allowed the spectroscopic mapping of the SWNTs present in the composite through microRaman microscopy. Transmission SNOM at sub-diffraction limits was also achieved on the composite, using the strong fluorescence signal. The fluorescence was observed for all metal nanoparticle composites such as gold nanoparticle (mean diameter 12 nm), silver nanoparticles (mean diameter 60 nm) and gold nanorods (mean diameter 11 nm, aspect ratio 2.8). However, it was not observed in pristine nanoparticles, nanorods or SWNTs. Thus, the fluorescence is attributed to the inherent states of modified SWNTs present in
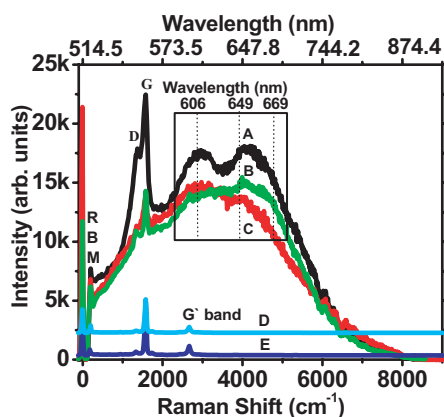

Fig. 10.   Raman spectra of Ag–SWNT composite (trace A), AuNR-SWNT (trace B) and Au-SWNT (trace C) composites. Trace D and E pertain to control experiments with pristine SWNTs and SWNTs heated with tridsodium citrate, respectively. The corresponding emission wavelengths are marked. The emission maxima occur at 606 and 652 nm. The RBM, D and G bands are marked.

the composite. The discovery poses important questions about the metallic states of SWNTs, which are bound to be present in the composite.

The presence of metallic states offer nano-radiative decay channels[32] and thus the near-infrared fluorescence, normally observed in isolated SWNTs is not usually observed in SWNT bundles.[32] Therefore, a thorough investigation of the electrical properties of the SWNTs in the composite was carried out using point-contact current-imaging atomic force microscopy (PCI-AFM) and microRaman spectroscopy. Metallic SWNTs (mSWNTs) isolated from an ensemble according to established procedures[33] were used to form the composite with metal nanoparticles. The PCI-AFM images of pristine mSWNTs and the composite are shown in Figs. 11(a) and 11(b), respectively. Differential conductance plots, reflecting the
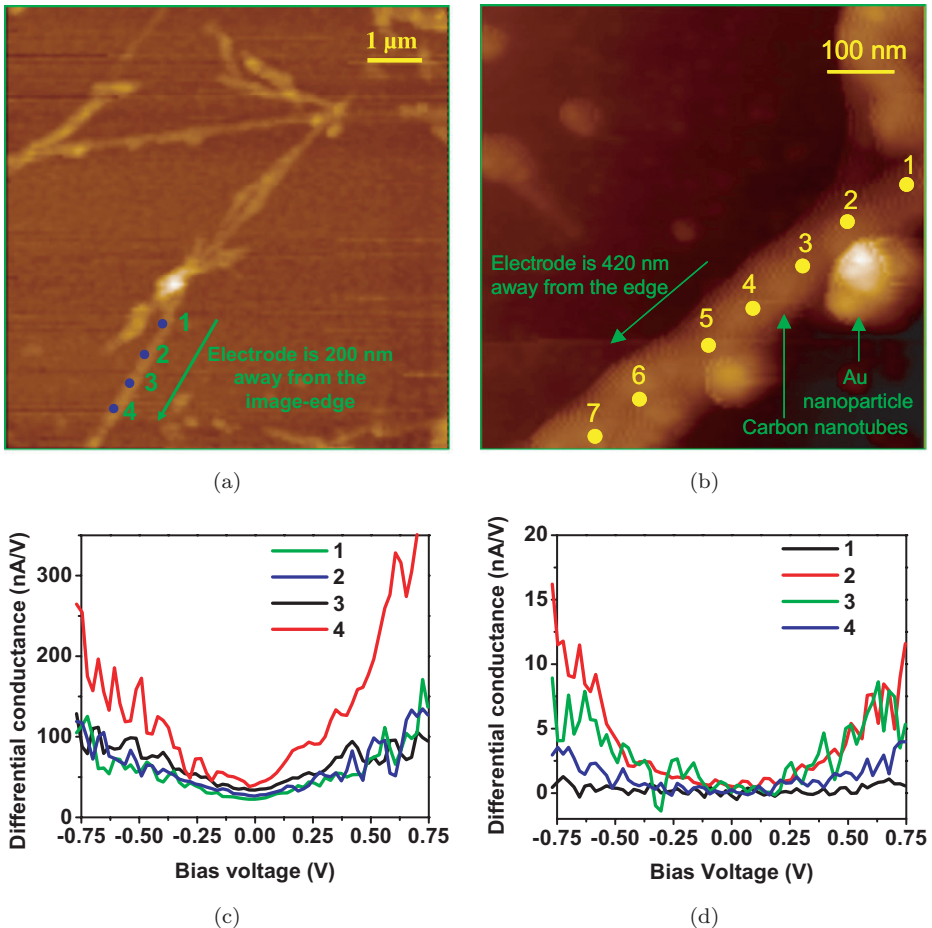

Fig. 11. PCI-AFM images of (a) pure mSWNT and (b) Au-mSWNT composite. The corresponding differential conductances measured at specific locations labeled 1 to 4 are shown in (c) and (d), respectively. Non-zero conductance values are seen in (c) at the Fermi point in comparison to (d) where zero conductance is seen.

density of states of SWNTs for mSWNTs and SWNT composite are shown in Figs. 11(c) and 11(d), respectively.

The conductance in the Fermi region for SWNT composite being zero, reflects the semiconducting states of the SWNTs in the composite. This is in contrast to the non-zero conductance near the Fermi region for mSWNTs, which is the starting material. Thus mSWNTs are converted to semiconducting SWNTs upon formation of the composite. Thus, a metal–semiconductor transition was observed in SWNTs due to interaction with metal nanoparticles. The nature of this interaction has been probed and established to be electrostatic in nature.

4. Conclusions

In this paper, we have reviewed our research on chemical interactions at noble metal surfaces in some detail. Simple halocarbons degrade at the surfaces of metal nanoparticles to metal halides and amorphous carbon at room temperature by a new chemistry, which offers a simple and effective methodology for environmental remediation. The new chemistry was exploited for devising a filter for the effective removal of common pesticide contaminants from drinking water. Immobilization of biologically important molecules such as hemin, Cyt *c*, hemoglobin and myoglobin on Au and Ag nanostructures lead to nano–bio conjugates and their surface binding chemistry was explored in detail. The nano–bio conjugates were characterized by spectroscopy and microscopy. Polymer–nano composites with tunable optical properties were prepared by single and multi-step methodologies and the utility of them in sensing was investigated. Smart nanogel–nanoparticle composites and nanogel–nanorod patterns were made from PNIPAM based on a template-assisted method. An array of noble metal nanostructures fabricated on conducting glass substrates showed excellent flow sensing characteristics by the transverse electrokinetic effect. Composites made from noble metal nanostructures and metallic single walled carbon nanotubes showed concomitant visible fluorescence and metal to semiconductor transition, as shown by Raman and PCI-AFM measurements.

References

1. Lu Y and Liu J, Smart nanomaterials inspired by biology: Dynamic assembly of error-free nanomaterials in response to multiple chemical and biological stimuli, *Acc Chem Res* **40**:315–323, 2007.
2. Lee BI, Qi L and Copeland T, Nanoparticles for materials design: Present & future, *J Ceram Process Res* **6**:31–40, 2005.

3. Daniel MC and Astruc D, Gold nanoparticles: Assembly, supramolecular chemistry, quantum-size-related properties and applications toward biology, catalysis, and nanotechnology, *Chem Rev* **104**:293–346, 2004.

4. Zhang WX, Nanoscale iron particles for environmental remediation: An overview, *J Nanopart Res* **5**:323–332, 2003.

5. Fan J and Gao Y, Nanoparticle-supported catalysts and catalytic reactions — A minireview, *J Exp Nanosci* **1**:457–475, 2006.

6. Mayer ABR, Colloidal metal nanoparticles dispersed in amphiphilic polymers, *Polym Adv Technol* **12**:96–106, 2001.

7. Son S, Park IK, Park J and Hyeon T, Synthesis of Cu_2O coated Cu nanoparticles and their successful applications to Ullmann-type amination coupling reactions of aryl chlorides, *Chem Commun* 778–779, 2004.

8. Crooks RM, Zhao M, Sun L, Chechik V and Yeung LK, Dendrimer-encapsulated metal nanoparticles: Synthesis, characterization and applications to catalysis, *Acc Chem Res* **34**:181–190, 2001.

9. Rahim EH, Kamounah FS, Frederiksen J and Christensen JB, Heck reactions catalyzed by PAMAM-dendrimer encapsulated Pd(0) nanoparticles, *Nano Lett* **1**:499–501, 2001.

10. Moreno-Manas M and Pleixats R, Formation of carbon–carbon bonds under catalysis by transition-metal nanoparticles, *Acc Chem Res* **36**:638–643, 2003.

11. Stevens PD, Fan J, Gardimalla HMR, Yen M and Gao Y, Superparamagnetic nanoparticle-supported catalysis of Suzuki cross-coupling reactions, *Org Lett* **7**:2085–2088, 2005.

12. Savage N and Diallo MS, Nanomaterials and water purification: Opportunities and challenges, *J Nanopart Res* **7**:331–342, 2005.

13. Coyle S, Wu SY, Lau KT, Rossi DD, Wallace G and Diamond D, Smart nanotextiles: A review of materials and applications, *Mater Res Bullt* **32**:434–442, 2007.

14. Nair AS and Pradeep T, Halocarbon mineralization and catalytic destruction by metal nanoparticles, *Curr Sci* **84**:1560–1564, 2003.

15. Nair AS, Tom RT, Suryanarayanan V and Pradeep T, ZrO_2 bubbles from core–shell nanoparticles, *J Mater Chem* **13**:297–300, 2003.

16. Suryanarayanan V, Nair AS, Tom RT and Pradeep T, Porosity of core–shell nanoparticles, *J Mater Chem* **14**:2661–2666, 2004.

17. Nair AS, Tom RT and Pradeep T, Detection and extraction of endosulfan by metal nanoparticles, *J Environ Monitor* **5**:363–365, 2003.

18. Nair AS and Pradeep T, Quantitative extraction of chlorpyrifos and malathion from water by metal nanoparticles, *J Nanosci Nanotechnol* **7**:1871–1877, 2007.

19. Tom RT and Pradeep T, Interaction of azide ion with hemin and Cyt *c* immobilized on Au and Ag nanoparticles, *Langmuir* **21**:11896–11902, 2005.

20. Tom RT, Samal AK, Sreeprasad TS and Pradeep T, Hemoprotein bioconjugates of Au and Ag nanoparticles and Au nanorods: Structure–function correlations, *Langmuir* **23**:1320–1325, 2007.

21. Rajeevkumar VR and Pradeep T, Polymerization of benzyl thiocyanate on silver nanoparticles and the formation of polymer coated nanoparticles, *J Mater Chem* **16**:837–841, 2006.

22. Rajeevkumar VR and Pradeep T (unpublished results).

23. Rajeevkumar VR and Pradeep T, Gold nanorods grown on microgels leading to hexagonal nanostructures, *Langmuir* **23**:8667–8669, 2007.

24. Subramaniam C, Tom RT and Pradeep T, On the formation of protected gold nanoparticles from $AuCl_4^-$ by the reduction using aromatic amines, *J Nanopart Res* **7**:209–217, 2005.

25. Subramaniam C, Pradeep T and Chakrabarti J, Flow induced transverse electrical potential across an assembly of gold nanoparticles, *Phys Rev Lett* **95**:164501–164504, 2005.

26. Subramaniam C, Pradeep T and Chakrabarti J, Transverse electrokinetic effect: A potential flow sensor, *J Phys Chem C* (in press).

27. Subramaniam C, Sreeprasad, TS, Pradeep T, Pavan Kumar GV, Narayana C, Yajima T, Sugawara Y, Tanaka H, Ogawa T and Chakrabarti J, Metal–semiconductor transition induced visible fluorescence in single walled carbon nanotubes–noble metal nanoparticle composites, *Phys Rev Lett* **99**:167404–167407, 2007.

28. Rose MJ, Mac Laren I and Pradeep T, Carbon onions within silica nanoshells, *Carbon* **42**:2352–2356, 2004.

29. Rosemary MJ, Suryanarayanan V, MacLaren I and Pradeep T, Aniline incorporated silica nanobubbles, *J Chem Sci* **118**:375–384, 2006.

30. Rosemary MJ, MacLaren I and Pradeep T, Investigations of the antibacterial properties of ciprofloxacin@SiO_2, *Langmuir* **22**:10125–10129, 2006.

31. Jackson JD, *Classical Electrodynamics*, Wiley Press, New York, 1998.

32. O'Connell MJ, Bachilo SM, Huffman CB, Moore VC, Strano MS, Haroz EH, Rialon KL, Boul PJ, Noon WH, Kittrell C, Ma J, Hauge RH, Weisman RB and Smalley RE, Band gap fluorescence from individual single-walled carbon nanotubes, *Science* **297**:593–596, 2002.

33. Maeda Y, Kimura SI, Kanda M, Hirashima Y, Hasegawa T, Wakahara T, Lian Y, Nakahodo T, Tsuchiya T, Akasaka T, Lu J, Zhang X, Gao G, Yu Y, Nagase S, Kazaoui S, Minami N, Shimizu T, Tokumoto H and Saito R, Large-scale separation of metallic and semiconducting single-walled carbon nanotubes, *J Am Chem Soc* **127**:10287–10290, 2005.